

Polarimetric SAR Interferometry

Shane Robert Cloude, *Member, IEEE*, and Konstantinos P. Papathanassiou

Abstract—In this paper, we examine the role of polarimetry in synthetic aperture radar (SAR) interferometry. We first propose a general formulation for vector wave interferometry that includes conventional scalar interferometry as a special case. Then, we show how polarimetric basis transformations can be introduced into SAR interferometry and applied to form interferograms between all possible linear combinations of polarization states. This allows us to reveal the strong polarization dependency of the interferometric coherence. We then solve the coherence optimization problem involving maximization of interferometric coherence and formulate a new coherent decomposition for polarimetric SAR interferometry that allows the separation of the effective phase centers of different scattering mechanisms. A simplified stochastic scattering model for an elevated forest canopy is introduced to demonstrate the effectiveness of the proposed algorithms. In this way, we demonstrate the importance of wave polarization for the physical interpretation of SAR interferograms. We investigate the potential of polarimetric SAR interferometry using results from the evaluation of fully polarimetric interferometric shuttle imaging radar (SIR)-C/X-SAR data collected during October 8–9, 1994, over the SE Baikal Lake Selenga delta region of Buriatia, Southeast Siberia, Russia.

Index Terms—Polarimetric interferometry, radar polarimetry, synthetic aperture radar (SAR), SAR interferometry.

I. INTRODUCTION

SYNTHETIC aperture radar (SAR) interferometry is an established technique to measure terrain topography [1], [2]. The application of this technique is based on the generation of an interferogram using two complex SAR images of the same area acquired from two slightly different look angles. The statistical phase contributions in both images due to speckle can be supposed to be the same (assuming the same imaging geometry and the same scene properties in both acquisitions) and thus cancels out when the phase difference, which contains information related to the scene topography, is determined. The two images can either be acquired by using two antennas on the same platform simultaneously (single-pass interferometry) or by using one antenna for repeat passes over the same area at two different times (repeat-pass interferometry).

The performance of an interferometric system depends on the radar sensor parameters, the accuracy of the flight-track estimation, and the quality of the data processing procedures. The fact that the interferometric phase can be measured only

modulo 2π makes the determination of the absolute phase necessary. The ability to resolve the 2π ambiguities depends on the local terrain slope and the phase noise level caused by signal decorrelation between the two acquired images [3]. This can be due to geometrical effects, whereby the difference of look angles causes a random change in the speckle pattern introducing noise in the interferometric phase estimation (baseline decorrelation). In the repeat-pass case, temporal decorrelation of the scene due to changes in the backscatter behavior between the two observations leads to a randomization of the phase, reducing the signal correlation.

Another potential application of SAR interferometry besides digital elevation model (DEM) generation is the extraction of physical parameters related to natural scattering mechanisms. Two factors constrain the evaluation of the relation between the interferometric observables and characteristic parameters of the scattering processes. The first is underdetermination of the inversion problem. Even using the simplest scattering models, a conventional interferometric system operating with a fixed polarization at a single frequency is not able to provide enough independent parameters necessary to describe natural scattering processes. The second is correct interpretation of the interferograms. A critical point is estimation of the location of the effective scattering phase centers, which depend on system parameters, such as wavelength and polarization, as well as on physical and geometrical parameters of the scatterer. The interpretation depends strongly on our understanding of the way in which different types of terrain interact with vector electromagnetic waves and how this interaction affects the backscattered radar signal.

To solve these problems, several multiparameter interferometric approaches have been proposed in the literature. Multitemporal techniques [4], [5] are based on the fact that variation of time resolution, given by the repeat-pass time interval, enables us to evaluate changing processes occurring on different time scales, and described by the amount of temporal decorrelation. Interferometric data collected continuously over a long time period can be employed to detect natural changing processes and relate them to different surface types, as well as to determine the influence of perturbations of the propagation medium (atmospheric effects).

Multibaseline approaches have been introduced to extend the number of independent observations [6]. They are also used to analyze geometrical influences on the interferometric coherence and facilitate the estimation of scatterer-relevant quantities [7], [8].

Multifrequency methods [4], [9] make use of the frequency-dependent behavior of the interferometric coherence and the different penetration properties of electromagnetic waves for

Manuscript received November 17, 1997; revised May 5, 1998. This work was supported by the Alexander von Humboldt Foundation, Bonn, Germany. S. R. Cloude is with Applied Electromagnetics, KY16 9UR St. Andrews Fife, U.K. (e-mail: scloude@fges.demon.co.uk).

K. P. Papathanassiou is with Deutsches Zentrum für Luft-und Raumfahrt (DLR), German Aerospace Center, D-82230 Oberpfaffenhofen, Germany (e-mail: kostas.papathanassiou@dlr.de).

Publisher Item Identifier S 0196-2892(98)06844-2.



Fig. 1. SAR images of the test area across the Selenga delta at SE Lake Baikal. (Tien Shan test site, latitude N 52.16°, longitude E 106.67°). (a) Total power image, (b) *HH* image, and (c) *LL* image.

different frequencies to improve the accuracy of the generated DEM's and extract physical information about the scattering processes even in the presence of vegetation.

In this paper, we examine the advantages of using radar polarimetry for the solution of such problems. Radar polarimetry is a valuable technique for the extraction of geophysical parameters from SAR images and terrain classification. The approaches to do this are either based on the statistical analysis of the polarimetric information [10]–[12] or on scattering models, which provide an understanding of the physics of the scattering processes [13]–[15], [37]. A new technique that permits the derivation of terrain slopes and elevations from a single polarimetric data set has been introduced in [16] and makes for the first time possible the extraction of topographic information using polarimetric techniques. Here we investigate the introduction of polarimetric techniques in interferometric applications to demonstrate how the analysis of interferometric scattering matrix data can improve the performance of conventional SAR interferometry. Section II summarizes some of the key points of conventional scalar SAR interferometry. A general vector formulation is proposed in Section III. Section IV describes how transformations of the polarimetric basis can be introduced into interferometry. A vectorial coherence optimization algorithm is described in Section V, followed by the application of a new coherent decomposition theorem to polarimetric interferometric data in Section VI. In Section VII, a stochastic scattering model is introduced to demonstrate the effectiveness of the optimization algorithm.

The experimental data used are L-band scattering matrix single-look complex (SLC) image pairs of the Tien Shan test

site acquired by the shuttle imaging radar (SIR)-C/X-SAR radar system on October 8 and 9, 1994 (data takes 122.20 and 154.20), and processed by NASA/Jet Propulsion Laboratory, Pasadena, CA. The test area is located close to the southeastern edge of Lake Baikal, Buriatia, Russia (latitude N 52.16°, longitude E 106.67°), and is a mixed forestry/agricultural area crossed by the Selenga River at its delta region (see Fig. 1).

II. SCALAR INTERFEROMETRY

Interferogram generation can be described as the formation of the average Hermitian product of two complex scalar signals s_1 and s_2 for the same resolution element received from two spatially separated antennas. Their spatial separation is called the baseline B . Of special significance in this context is the 2×2 Hermitian positive semidefinite coherency matrix $[J]$, which we define as

$$[J] := \left\langle \begin{bmatrix} s_1 \\ s_2 \end{bmatrix} \begin{bmatrix} s_1^* & s_2^* \end{bmatrix} \right\rangle = \begin{bmatrix} \langle s_1 s_1^* \rangle & \langle s_1 s_2^* \rangle \\ \langle s_2 s_1^* \rangle & \langle s_2 s_2^* \rangle \end{bmatrix} \quad (1)$$

where $*$ means complex conjugation and $\langle \dots \rangle$ indicates the expectation value. From $[J]$, we can obtain an expression for the phase of the interferogram $\phi = \arg(s_1 s_2^*)$ as

$$\phi = \arctan\left(\frac{\text{Im}\{s_1 s_2^*\}}{\text{Re}\{s_1 s_2^*\}}\right) + 2\pi N, \quad N = (0, \pm 1, \pm 2, \dots). \quad (2)$$

ϕ contains both range and topography-dependent information. The interferometric coherence γ is defined as the absolute value of the normalized complex cross correlation between both signals

$$\gamma_{\text{Int}} = \frac{|\langle s_1 s_2^* \rangle|}{\sqrt{\langle s_1 s_1^* \rangle \langle s_2 s_2^* \rangle}}, \quad 0 \leq \gamma \leq 1 \quad (3)$$

and is a measure of the phase noise of the interferogram. Importantly, the achievable accuracy of the estimation of the interferometric phase is reduced by any loss in coherence. Assuming phase preserving SAR and interferometric processing, the interferometric coherence can be modeled as a composition of the following contributions:

$$\gamma_{\text{Int}} = \gamma_{\text{SNR}} \cdot \gamma_{\text{Baseline}} \cdot \gamma_{\text{Temporal}}. \quad (4)$$

- γ_{SNR} represents the decorrelation caused by additive noise. Assuming the same signal-to-noise ratio (SNR) in both images, γ_{SNR} is given by [17]

$$\gamma_{\text{SNR}} = \frac{1}{1 + (\text{SNR})^{-1}}. \quad (5)$$

The influence of γ_{SNR} is restricted mainly to areas characterized by a low backscattering behavior.

- γ_{Baseline} expresses decorrelation due to perspective changes caused by the spatial separation of the two antennas. The two SAR images acquired from different look angles contain different bands of the complex reflectivity spectrum [18]. In the case of pure surface scattering, the decorrelation can be eliminated by common spectral band filtering of the range spectra [19]. However, any finite height distribution of the scatterers inside the resolution cell leads to spectral decorrelation (volume decorrelation) that cannot be removed by applying spectral filtering [20].
- γ_{Temporal} is the temporal decorrelation caused by changes in the scatterer geometry and/or the backscattering behavior of the scatterers within the resolution cell occurring during the time interval between the two acquisitions.

While γ_{SNR} can be considered to be independent of polarization, because noise does not have any polarimetric structure, the other two contributions γ_{Baseline} and γ_{Temporal} are strongly dependent on wave polarization, as we show in the next sections.

III. VECTOR INTERFEROMETRY

Fully polarimetric radar systems measure 2×2 complex scattering matrix $[S]$ samples for each resolution element in the image [21]. To generalize the expressions for the interferometric phase and coherence, we utilize the coherent scattering vector \underline{k} equivalent to a vectorization of the scattering matrix $[S]$

$$\begin{aligned} \underline{k} &= \frac{1}{2} \text{Trace}([S] \Psi_P) \\ &= \frac{1}{\sqrt{2}} [S_{HH} + S_{VV}, S_{VV} - S_{HH}, \\ &\quad S_{HV} + S_{VH}, i(S_{HV} - S_{VH})]^T. \end{aligned} \quad (6)$$

T indicates the matrix transposition operation, and S_{ij} ($i, j = H$ or V) is the complex scattering coefficient for j transmitted and i received polarization in the HV -polarimetric basis. Ψ_P is the set of 2×2 orthogonal complex

Pauli basis matrices

$$\Psi_P = \left\{ \sqrt{2} \begin{bmatrix} 1 & 0 \\ 0 & 1 \end{bmatrix}, \sqrt{2} \begin{bmatrix} 1 & 0 \\ 0 & -1 \end{bmatrix}, \sqrt{2} \begin{bmatrix} 0 & 1 \\ 1 & 0 \end{bmatrix}, \sqrt{2} \begin{bmatrix} 0 & -i \\ i & 0 \end{bmatrix} \right\}. \quad (7)$$

For the vectorization of $[S]$, different orthogonal basis sets can be used [15]. The advantage of using the Pauli matrix basis is that the elements of the resulting scattering vector are closely related to the physics of wave scattering and allow a better interpretation of the scattering mechanisms [22]. In the case of backscattering in a reciprocal medium, the reciprocity theorem constrains the scattering matrix to be complex symmetric, i.e., $S_{HV} = S_{VH}$, and, instead of the four-dimensional (3-D) vector of (6), a reduced three-dimensional (3-D) scattering vector can be used

$$\underline{k} = \frac{1}{\sqrt{2}} [S_{HH} + S_{VV}, S_{VV} - S_{HH}, 2S_{HV}]^T. \quad (8)$$

Using the outer product formed from the scattering vectors \underline{k}_1 and \underline{k}_2 for images I1 and I2, we can define a 6×6 Hermitian positive semidefinite matrix $[T_6]$

$$[T_6] := \left\langle \begin{bmatrix} \underline{k}_1 \\ \underline{k}_2 \end{bmatrix} \begin{bmatrix} \underline{k}_1^{*T} & \underline{k}_2^{*T} \end{bmatrix} \right\rangle = \begin{bmatrix} [T_{11}] & [\Omega_{12}] \\ [\Omega_{12}]^{*T} & [T_{22}] \end{bmatrix} \quad (9)$$

where $[T_{11}]$, $[T_{22}]$, and $[\Omega_{12}]$ are 3×3 complex matrices given by

$$\begin{aligned} [T_{11}] &= \langle \underline{k}_1 \underline{k}_1^{*T} \rangle \\ [T_{22}] &= \langle \underline{k}_2 \underline{k}_2^{*T} \rangle \\ [\Omega_{12}] &= \langle \underline{k}_1 \underline{k}_2^{*T} \rangle. \end{aligned} \quad (10)$$

$[T_{11}]$ and $[T_{22}]$ are the standard Hermitian coherency matrices that contain the full polarimetric information for each separate image. $[\Omega_{12}]$ is a new 3×3 complex matrix that contains not only polarimetric information, but also the interferometric phase relations of the different polarimetric channels between both images. It is important to note that while $[T_6]$ is Hermitian positive, semidefinite by definition, $[\Omega_{12}]$ is not. The phase difference between \underline{k}_1 and \underline{k}_2 is caused by different ranges to the resolution cell as well as to possible temporal changes. Hence, in general, $\underline{k}_1 \neq \underline{k}_2$ and, consequently, $\langle \underline{k}_1 \underline{k}_2^{*T} \rangle \neq \langle \underline{k}_2 \underline{k}_1^{*T} \rangle$.

To extend the scalar formulation into a vectorial one, we introduce two normalized complex vectors \underline{w}_1 and \underline{w}_2 that can be interpreted as two scattering mechanisms (see Appendix A). We define scattering coefficients μ_1 and μ_2 as the projection of the scattering vectors \underline{k}_1 and \underline{k}_2 onto the vectors \underline{w}_1 and \underline{w}_2 , respectively

$$\mu_1 = \underline{w}_1^{*T} \underline{k}_1, \quad \mu_2 = \underline{w}_2^{*T} \underline{k}_2. \quad (11)$$

The scalar functions μ_1 and μ_2 are linear combinations of the elements of the scattering matrices $[S_1]$ and $[S_2]$, and they form the basis for the generation of vector interferograms. Equation (11) can now be combined with (9) to derive a 2×2 Hermitian positive, semidefinite coherency matrix $[J]$

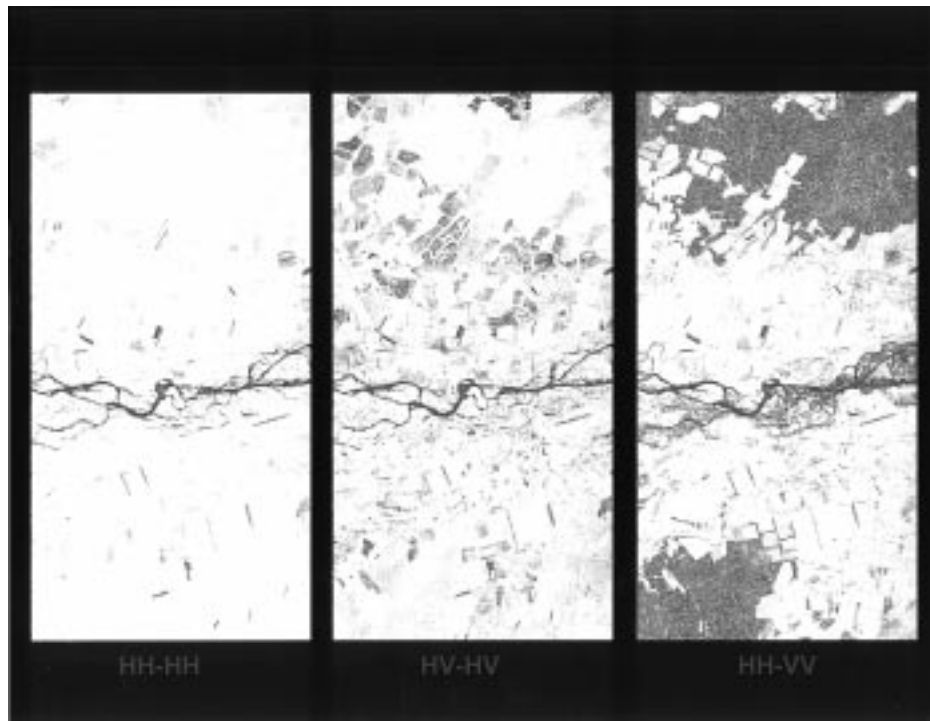


Fig. 2. Coherence maps of interferograms in the (H, V) -polarization basis (Left: $HH-HH$. Middle: $HV-HV$. Right: $HH-VV$).

for the vector case [analogous to the scalar formulation in (1)] from the 6×6 matrix $[T_6]$

$$[J] = \left\langle \begin{bmatrix} \mu_1 \\ \mu_2 \end{bmatrix} \begin{bmatrix} \mu_1^* & \mu_2^* \end{bmatrix} \right\rangle = \begin{bmatrix} \underline{w}_1^{*T} [T_{11}] \underline{w}_1 & \underline{w}_1^{*T} [\Omega_{12}] \underline{w}_2 \\ \underline{w}_2^{*T} [\Omega_{12}]^* \underline{w}_1 & \underline{w}_2^{*T} [T_{22}] \underline{w}_2 \end{bmatrix}. \quad (12)$$

Combining now (11) with (10), we obtain an expression for vector interferogram formation as

$$\mu_1 \mu_2^* = (\underline{w}_1^{*T} \underline{k}_1) (\underline{w}_2^{*T} \underline{k}_2)^* = \underline{w}_1^{*T} [\Omega_{12}] \underline{w}_2 \quad (13)$$

from which we can derive the interferometric phase as

$$\phi_i = \arg(\underline{w}_1^{*T} \underline{k}_1 \underline{k}_2^* \underline{w}_2) = \arg(\underline{w}_1^{*T} [\Omega_{12}] \underline{w}_2). \quad (14)$$

The generalized vector expression for the coherence γ is then given by

$$\gamma = \frac{|\langle \underline{w}_1^{*T} [\Omega_{12}] \underline{w}_2 \rangle|}{\sqrt{\langle \underline{w}_1^{*T} [T_{11}] \underline{w}_1 \rangle \langle \underline{w}_2^{*T} [T_{22}] \underline{w}_2 \rangle}}. \quad (15)$$

It is important to realize that the last equation is a more general expression for the interferometric coherence than the conventional scalar expression in (4). If $\underline{w}_1 \neq \underline{w}_2$, we have, in addition to the different interferometric contributions γ_{Int} , the contribution of the polarimetric correlation γ_{Pol} between the two scattering mechanisms corresponding to \underline{w}_1 and \underline{w}_2

$$\gamma = \gamma_{\text{Int}} \cdot \gamma_{\text{Pol}}. \quad (16)$$

Only in the special case of $\underline{w}_1 = \underline{w}_2$ does γ_{Pol} become one and $\gamma = \gamma_{\text{Int}}$.

Fig. 1(a) shows the total polarimetric power image [i.e., $1/2(|S_{HH}|^2 + 2|S_{HV}|^2 + |S_{VV}|^2)$] of the test site, and Fig. 1(b) shows the HH -polarized SLC image. In Fig. 2, the coherence maps of three interferograms formed by using different linear combinations of elements of the scattering vectors in the (H, V) -basis are shown. The scaling from white to black corresponds to the coherence range from one to zero. Comparison of the three coherence maps demonstrates clearly the effect of the different sources of decorrelation.

In the $HH-HH$ map ($\underline{w}_1 = \underline{w}_2 = [1/\sqrt{2}, -1/\sqrt{2}, 0]^T$), a significant loss in coherence is observable only on the river and a few other water covered areas, mainly due to temporal decorrelation. From (16), it follows that, in areas which have a high temporal decorrelation, the coherence will remain low, independently of the choice of polarization. Over the forested areas, located at the northern and southern parts of the test area, the loss in coherence is caused mainly by volume decorrelation resulting from the height distribution of the effective scatterers in the resolution cell. In the $HV-HV$ map ($\underline{w}_1 = \underline{w}_2 = [0, 0, 1]^T$), the high decorrelation over the shrubland areas, located around the river, is pure noise decorrelation due to the low SNR resulting from the low HV -backscattering coefficient characteristic of smooth, dominant surface scatterers. In the $HH-VV$ map ($\underline{w}_1 = [1/\sqrt{2}, -1/\sqrt{2}, 0]^T$ and $\underline{w}_2 = [1/\sqrt{2}, 1/\sqrt{2}, 0]^T$), the reason for the observed total decorrelation over the forested areas is predominantly polarimetric decorrelation between the HH - and VV -polarized backscattered signals from areas dominated by volume scattering. The corresponding coherence histograms, shown in Fig. 3, give a quantitative comparison

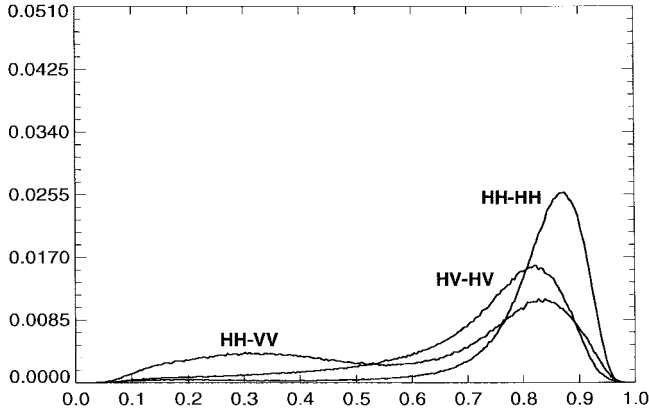


Fig. 3. Coherence histograms in the (H, V) -polarization basis.

of the polarization-dependent coherence behavior in the three interferograms.

IV. POLARIMETRIC BASIS TRANSFORMATION

The knowledge of the scattering matrix in one polarization basis allows us to derive the scattering matrix in any other orthogonal (A, B) -basis by the following unitary congruence matrix transformation [23], [24]:

$$[S]_{AB} = [U_2][S]_{HV}[U_2]^T \quad (17)$$

where the three-parameter transformation matrix $[U_2]$ has the form

$$[U_2] = \begin{bmatrix} \exp(i\tilde{\phi}/2) & 0 \\ 0 & \exp(-i\tilde{\phi}/2) \end{bmatrix} \cdot \begin{bmatrix} \cos \alpha & \sin \alpha \exp i\delta \\ -\sin \alpha \exp -i\delta & \cos \alpha \end{bmatrix}. \quad (18)$$

α and δ are the Deschamps parameters of the polarization state [25] on the Poincaré sphere. The matrix $[U_2]$ is special unitary, which means that as well as being unitary it also has unit determinant. These two constraints are required to ensure that the amplitude of the wave remains independent of the choice of the basis and the phase of the wave may be consistently defined as we change the polarization basis. The definition of phase is very important for interferometry and (18) shows that, if we wish to change the phase of the basis polarization state A by an angle $\tilde{\phi}/2$, we must change the phase of the orthogonal B component by the negative of this angle. This permits us to define any complex polarization A with absolute phase, determine a unique orthogonal wave B , and construct a new basis that we can use to express the complex scattering elements of the measured matrix $[S_{HV}]$. The absolute knowledge of the phase reference $\tilde{\phi}$ is not important because it is not characteristic of the polarization state of the wave. Normally, in radar polarimetry, the phase reference is taken as $\tilde{\phi} = 0$. From the interferometric point of view, it is important to use the same phase for the transformation of both images.

Assuming $\tilde{\phi} = 0$, we can write the unitary matrix $[U_2]$ in terms of a single complex parameter known as the complex polarization ratio, which describes the change of polarization

base [26], [37]

$$\rho = \tan \alpha \exp i\delta \quad (19)$$

in which case (16) can be written as

$$[U_2] = \frac{1}{\sqrt{1+\rho\rho^*}} \begin{bmatrix} 1 & \rho \\ -\rho^* & 1 \end{bmatrix}. \quad (20)$$

The corresponding transformation of the scattering vector \underline{k}_{HV} is given by [15]

$$\underline{k}_{AB} = [U_3]\underline{k}_{HV} \quad (21)$$

with

$$[U_3] = \frac{1}{2(1+\rho\rho^*)} \cdot \begin{bmatrix} 2+\rho^2+\rho^{*2} & \rho^{*2}-\rho^2 & 2(\rho-\rho^*) \\ \rho^2-\rho^{*2} & 2-(\rho^2+\rho^{*2}) & 2(\rho+\rho^*) \\ 2(\rho-\rho^*) & -2(\rho+\rho^*) & 2(1-\rho\rho^*) \end{bmatrix} \quad (22)$$

where $[U_3]$ is a 3×3 special unitary matrix [which can be easily verified by showing that $[U_3][U_3]^*{}^T = [I]$ and $\det([U_3]) = 1$]. Physically, $[U_3]$ -transformations correspond to changes in the selected scattering mechanism in the image [15] and have been used for the interpretation of single-look multipolarization SAR data [23]. Here, we will examine their use in vector interferometry.

The possibility of transforming the scattering vector into any orthogonal polarimetric basis allows us to form interferograms between all possible elliptical polarization states on the Poincaré sphere. After transforming both scattering vectors from the (H, V) -basis into the (A, B) -basis, we obtain the complex scattering coefficients corresponding to the polarizations in the new basis. By forming the projection of the scattering vectors \underline{k}_{AB_i} onto normalized complex vectors \underline{w}_i , we obtain

$$\mu_i = \underline{w}_i^*{}^T \underline{k}_{AB_i} = \underline{w}_i^*{}^T [U_3] \underline{k}_{HV_i}. \quad (23)$$

The interferogram formation is then described by

$$\begin{aligned} \mu_1 \mu_2^* &= (\underline{w}_1^*{}^T [U_3] \underline{k}_{HV_1}) (\underline{w}_2^*{}^T [U_3] \underline{k}_{HV_2})^*{}^T \\ &= \underline{w}_1^*{}^T [U_3] [\Omega_{12}] [U_3]^*{}^T \underline{w}_2. \end{aligned} \quad (24)$$

Comparing the last equation with (13), we recognize that interferogram formation in any polarization basis can be described by a unitary similarity transformation of the $[\Omega_{12}]$ matrix.

To demonstrate that polarimetric basis transformations are phase-preserving transformations suitable for SAR interferometry, we transform the scattering matrix data, measured in the (H, V) -basis, into the important basis of left-right-hand circular polarization $[(L, R)$ -basis]. Setting $\rho = i$ in (22) [27], we can, using (21), express the scattering vector in the (L, R) -basis as a linear combination of the elements of the scattering matrix in the (H, V) -basis

$$\begin{aligned} \underline{k}_{LR} &= [U_3] \underline{k}_{HV} \\ &= \frac{1}{\sqrt{2}} [2iS_{HV}, S_{HH} - S_{VV}, i(S_{HH} + S_{VV})]^T. \end{aligned} \quad (25)$$

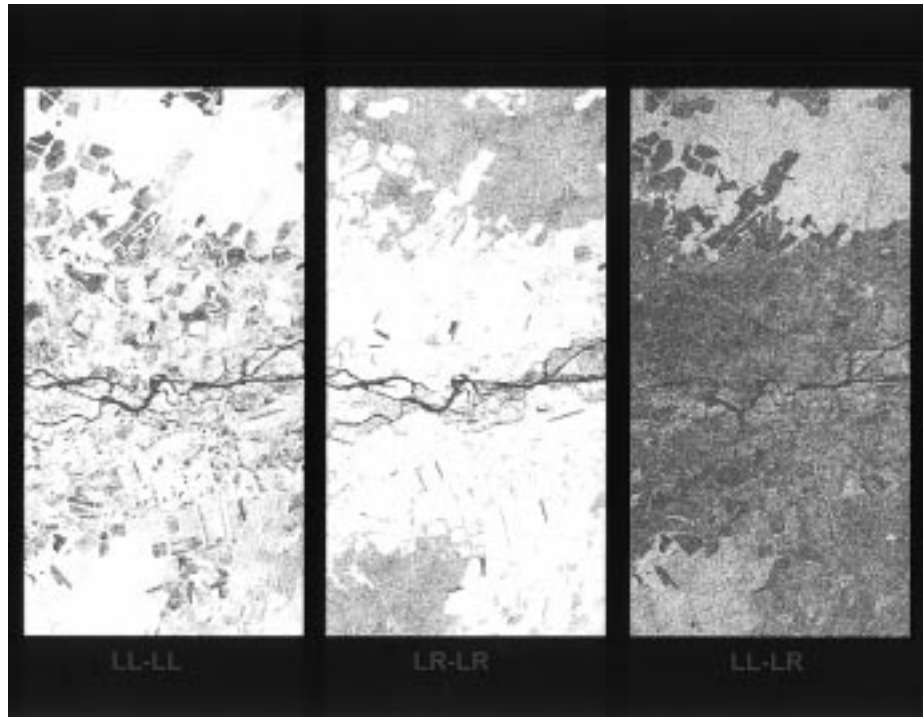


Fig. 4. Coherence maps of interferograms in the (L, R) -polarization basis (Left: $LL-LL$. Middle: $LR-LR$. Right: $LL-LR$).

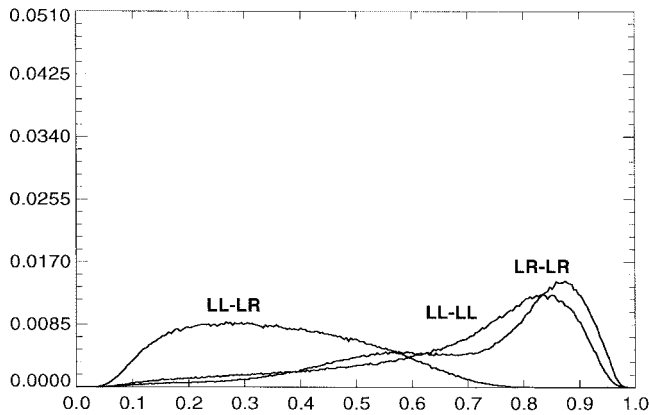


Fig. 5. Coherence histograms in the (L, R) -polarization basis.

The corresponding scattering matrix can be derived using (17). Fig. 1(c) shows the LL -polarized SLC image. In Fig. 4, the coherence maps of three interferograms formed by using different combinations of the elements of the scattering matrix in the (L, R) -basis are shown. The corresponding coherence histograms are shown in Fig. 5.

Note that an important feature in the interpretation of such images is polarimetric calibration of the scattering matrix data [28]–[30]. Polarimetric basis transformations require copolar and cross-polar complex calibration, and so the estimation of the copolar phase and the symmetrization scheme employed plays a key role in the data analysis. This is especially true in interferometric applications, in which not only the phase between elements of one scattering matrix is important, but also the relative phase between two scattering matrices is required. Phase calibration requirements in polarimetric interferometry are therefore more stringent than in conventional polarimetric applications.

V. COHERENCE OPTIMIZATION

The strong dependency of the interferometric coherence on the polarization, as demonstrated in the previous section, forces us to consider the question of which linear combination of polarization states yield the highest coherence. While much work has been carried out on optimization in polarimetry [31], all of it has been addressed to the single image or noncoherent cases. To solve the interferometric optimization problem, we need to formulate a coherent (i.e., phase preserving) optimization method.

The problem is to optimize the general vector formulation of the interferometric coherence as given in (15). Mathematically, we can do this by maximizing the complex Lagrangian L defined as

$$L = \underline{w}_1^{*T} [\Omega_{12}] \underline{w}_2 + \lambda_1 (\underline{w}_1^{*T} [T_{11}] \underline{w}_1 - C_1) + \lambda_2 (\underline{w}_2^{*T} [T_{22}] \underline{w}_2 - C_2) \quad (26)$$

where λ_1 and λ_2 are Lagrange multipliers introduced so that we can maximize the numerator of (15) while keeping the denominator constant. We can solve this maximization problem by setting the partial derivatives to zero

$$\begin{aligned} \frac{\partial L}{\partial \underline{w}_1^{*T}} &= [\Omega_{12}] \underline{w}_2 + \lambda_1 [T_{11}] \underline{w}_1 = 0 \\ \frac{\partial L}{\partial \underline{w}_2^{*T}} &= [\Omega_{12}]^* \underline{w}_1 + \lambda_2 [T_{22}] \underline{w}_2 = 0 \end{aligned} \quad (27)$$

and we obtain two 3×3 complex eigenvalue problems with common eigenvalues $\nu = \lambda_1 \lambda_2^*$

$$\begin{aligned} [T_{22}]^{-1} [\Omega_{12}]^* [T_{11}]^{-1} [\Omega_{12}] \underline{w}_2 &= \nu \underline{w}_2 \\ [T_{11}]^{-1} [\Omega_{12}] [T_{22}]^{-1} [\Omega_{12}]^* \underline{w}_1 &= \nu \underline{w}_1. \end{aligned} \quad (28)$$

The two matrices in (28) are not Hermitian, but we will show that they have real nonnegative eigenvalues. The maximum coherence value is then given by the square root of the maximum eigenvalue

$$\gamma_{\max} = \sqrt{\nu_{\max}}. \quad (29)$$

With ν_{\max} , we obtain $\underline{w}_{1\text{opt}}$ and $\underline{w}_{2\text{opt}}$ as the corresponding eigenvectors in (28). These are the optimum scattering mechanisms. To find the interferogram with the highest possible coherence, we project the scattering vectors \underline{k}_1 and \underline{k}_2 onto $\underline{w}_{1\text{opt}}$ and $\underline{w}_{2\text{opt}}$ to derive the two optimized scalar complex images $\mu_{1\text{opt}}$ and $\mu_{2\text{opt}}$ and form the interferogram between them

$$\begin{aligned} \mu_{1\text{opt}} \mu_{2\text{opt}}^* &= (\underline{w}_{1\text{opt}}^* \underline{k}_1) (\underline{w}_{2\text{opt}}^* \underline{k}_2)^* \\ &= \underline{w}_{1\text{opt}}^* [\Omega_{12}] \underline{w}_{2\text{opt}}. \end{aligned} \quad (30)$$

In Appendix B, we give an alternative interpretation of the optimization problem based on the singular value decomposition (SVD) method, which we use to show that matrices of the form $[T_{22}]^{-1} [\Omega_{12}]^* [T_{11}]^{-1} [\Omega_{12}]$ have real nonnegative eigenvalues. [To avoid any confusion between eigenvalues we will refer to the optimum values in (28) as singular values with corresponding singular vectors.]

The existence of solutions in (28) depends on the existence of the inverse matrices $[T_{11}]^{-1}$ and $[T_{22}]^{-1}$. This is not a severe constraint as in practice image coherency matrices are generally of full rank 3. If, however, there happens to be a strongly polarized signal and the covariance matrices are of rank 2 or less, the above formulation can be reworked using only the nonzero signal subspace. In the limit, if $[T_{11}]$ and $[T_{22}]$ are both rank 1, the scattering process can be described by a single effective scattering matrix and we can reduce the problem to a scalar problem like (3). In this special case, polarimetry makes no difference to the coherence optimization process.

However, one note of caution is required. The absolute phase of the singular vectors is not uniquely defined by (28), and so we must add an additional condition that fixes the phase difference between $\underline{w}_{1\text{opt}}$ and $\underline{w}_{2\text{opt}}$ uniquely. One approach would be to set the phase of one element of the vectors, for example, the first element, to be zero. However, this is unsatisfactory since in some circumstances this element may be zero. Looking at (30), we see that physically all interferometric phase information should be contained in $\underline{k}_1 \underline{k}_2^*$ and, hence, a sensible constraint is to require

$$\arg(\underline{w}_{1\text{opt}}^* \underline{w}_{2\text{opt}}) = 0. \quad (31)$$

This condition is automatically satisfied for $\underline{w}_{1\text{opt}} = \underline{w}_{2\text{opt}}$.

It is important to realize that these are not the same optimum states as are well known in single-imagery polarimetric optimization work [37]. Polarimetric signal-to-noise optimization of both images plays only a secondary role in the solution of the coherence optimization problem because it takes into account only the contribution of γ_{SNR} . Polarimetric contrast enhancement [32] is also based only on the optimization of the power ratios between two or more classes of scatterers and takes into account only $[T_{11}]$ and $[T_{22}]$, ignoring coherent

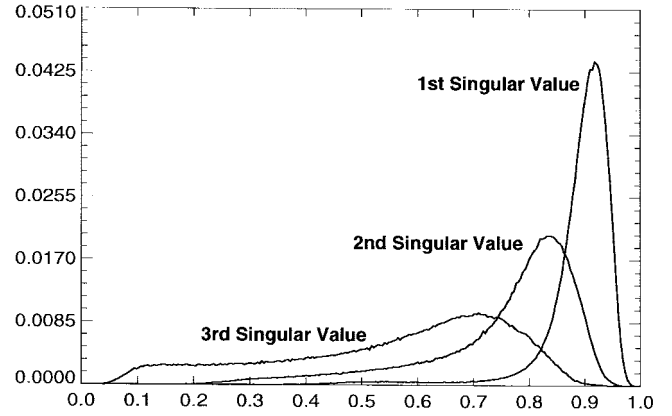


Fig. 6. Coherence histograms of the optimized interferograms.

effects that are contained in $[\Omega_{12}]$. The proposed coherent algorithm deals mainly with the two important decorrelation contributions γ_{Baseline} and γ_{Temporal} . Physically, the operation of the coherence optimization can be understood as the extraction of a deterministic scattering mechanism that has the closest possible relation to a “point-scatterer” from the data to reduce the height distribution of the effective scattering centers in the resolution cell to a point. In this way, we are able to remove the remaining volume decorrelation contribution in γ_{Baseline} .

In the absence of temporal decorrelation, the optimal scattering mechanisms will be the same for both images ($\underline{w}_1 = \underline{w}_2$). Temporal changes, i.e., changes in the scattering geometry within the resolution cell, will attempt to be compensated by variation of the polarization status in each image ($\underline{w}_1 \neq \underline{w}_2$), taking into account a loss in polarimetric correlation to increase γ_{Temporal} . The limitation is given by the amount of temporal decorrelation. If the temporal decorrelation is too high, the optimization algorithm cannot provide any improvement as the coherence will remain low, independently of the choice of polarization. Fig. 6 shows the three optimized coherence histograms for the SIR-C data of Fig. 1. A interpretation will be given in the next section.

VI. COHERENT SCATTERING DECOMPOSITION

In the last section, we used (28) to derive the optimum scattering mechanism in order to maximize the interferometric coherence. In this section, we will use the same equation to formulate a new kind of coherent target decomposition [15].

Equation (28) contains a pair of 3×3 complex eigenvalue equations, which consequently yield three singular values ν_j , with $\nu_1 \geq \nu_2 \geq \nu_3 \geq 0$, each related to a pair of singular vectors \underline{w}_{ij} , one for each image ($i = 1, 2$). The first vector pair $\{\underline{w}_{11}, \underline{w}_{21}\}$ related to the highest singular value represent the optimum scattering mechanisms, derived in the complete 3-D complex space of the vectors \underline{k}_i . The second pair $\{\underline{w}_{12}, \underline{w}_{22}\}$, belonging to the second highest singular value, can be interpreted as the optimum scattering mechanisms derived in the 2-D subspace orthogonal to the singular vectors of the first pair. Analogously, the third pair $\{\underline{w}_{13}, \underline{w}_{23}\}$, related to the lowest singular value, represent the optimum scattering

mechanisms in a one-dimensional (1-D) subspace orthogonal to the 2-D space generated by the vectors of the first two pairs. This allows us to express the matrices in (28) as the sum of three components, each one weighted by its appropriate singular value

$$\begin{aligned} [T_{11}]^{-1}[\Omega_{12}][T_{22}]^{-1}[\Omega_{12}]^{*T} \\ = \nu_1(\underline{w}_{11}\underline{w}_{11}^{*T}) + \nu_2(\underline{w}_{12}\underline{w}_{12}^{*T}) + \nu_3(\underline{w}_{13}\underline{w}_{13}^{*T}) \\ [T_{22}]^{-1}[\Omega_{12}]^{*T}[T_{11}]^{-1}[\Omega_{12}] \\ = \nu_1(\underline{w}_{21}\underline{w}_{21}^{*T}) + \nu_2(\underline{w}_{22}\underline{w}_{22}^{*T}) + \nu_3(\underline{w}_{23}\underline{w}_{23}^{*T}). \end{aligned} \quad (32)$$

Equation (32) constitutes an interferometric coherent decomposition theorem into six scattering mechanisms, three for Image 1 given by \underline{w}_{1j} and three for Image 2 given by \underline{w}_{2j} . The singular vectors \underline{w}_{1j} and \underline{w}_{2j} are in a special basis orthonormal (see Appendix B), a fact that can be physically interpreted as statistical independence between the scattering mechanisms. This approach can now be used to form three interferograms, each one related to a scattering mechanism independent from the others

$$\mu_{1j}\mu_{2j}^* = (\underline{w}_{1j}^{*T}\underline{k}_1)(\underline{w}_{2j}^{*T}\underline{k}_2)^{*T} = \underline{w}_{1j}^{*T}[\Omega_{12}]\underline{w}_{2j}. \quad (33)$$

The phase difference between these interferograms represents then the topographic phase difference between the effective phase centers of the related scattering mechanisms

$$\Delta\Phi_{ij} = \arg((\mu_{1i}\mu_{2i}^*)) - \arg((\mu_{1j}\mu_{2j}^*)). \quad (34)$$

The main difference between the proposed interferometric decomposition and other coherent decomposition theories, addressed in radar polarimetry [15], [33], is that the obtained scattering mechanism \underline{w}_{ij} are optimized with respect to the interferometric coherence. This means that the interferograms formed by using the optimized scattering mechanisms have the highest possible coherence, permitting the most accurate estimation of the phase difference between them.

Fig. 7 shows the coherence maps of the three interferograms formed by means of (33) using the three scattering mechanism pairs derived and applying the decomposition of (32). The fact that the coherence values are given by the related singular values makes evident that the three maps express the relative contributions of each scattering mechanism. We can recognize that areas with a dominant surface-scattering contribution are characterized by $\nu_1 \gg \nu_2 \approx \nu_3 \approx 0$ behavior of their singular values. Mathematically, this means that the corresponding coherency matrices are of rank 1, and physically, it leads to the conclusion of the presence of only one dominant scattering mechanism. The comparison with the $HH-HH$ coherence map in Fig. 2 makes it clear that in this case polarimetry does not have a strong influence on the interferometric coherence. More interesting are the forested areas that show a behavior close to $\nu_1 \approx \nu_2 \approx \nu_3$ of their singular values, an indicator of the existence of three pairs of independent scattering mechanisms. For this case, we can apply the interferometric decomposition to estimate the phase that corresponds to the height difference between the scattering centers in each interferogram. Fig. 8(a) shows the image of the extracted phase difference, and Fig. 8(b) shows the height

rescaled phase difference profile corresponding to the marked azimuthal line. The height variations over the forested areas are in the order of 20–30 m. Fig. 9 gives a 3-D view of the extracted phase difference. Although accurate ground truth data are not available, we suggest that this is directly a DEM of the canopy height of the forest. To support this, we now develop a canopy model that may be used to simulate such a scenario.

VII. CANOPY PENETRATION MODEL

In this section, we introduce a simplified electromagnetic model for the backscatter of radar signals from forestry and other vegetation. This model is intended to illustrate the significant role polarimetry can play in interferometric applications. It is to be made as simple as possible, yet it must contain sufficient complexity to represent the polarimetric behavior of a volume. For this reason, we reject at this stage a full vector transport approach, although such models are useful for more detailed analyses [34], [35]. Instead, we adopt a simplified three-level scattering model that will nonetheless contain enough physics to demonstrate the key ideas of polarimetric interferometry.

Fig. 10(a) shows schematically the key elements of the model. We assume that a wave propagates through a vegetation layer of thickness \underline{r}_1 and then interacts with a scatterer that may be the ground, a point scatterer or a ground-trunk interaction. For the vegetation canopy, we assume a tenuous particle cloud model but allow the particle scattering to vary with \underline{r} and be anisotropic in shape and have different orientation distributions. We further assume that the hidden scatterer is characterized by its position \underline{r}_T and scattering matrix $[S_T]$.

To obtain a vector interferometric model, we need an explicit expression for the 6×6 Hermitian matrix $[T_6]$. This we can generate in three stages, as follows.

- *Stage 1* expresses the propagation of the wave from the radar down to range $\underline{r} = \underline{r}_0$ through a homogeneous but anisotropic medium and will be described by a 2×2 complex propagation matrix $[P_2]$ [36].
- *Stage 2* describes the wave backscattering at $\underline{r} = \underline{r}_0$ by a coherent vector random process characterized by the scattering matrix $[S_V]$ and at $\underline{r} = \underline{r}_T$ by a deterministic scattering process characterized by the scattering matrix $[S_T]$.
- *Stage 3* propagates the scattered wave back to the radar using the transpose of the propagation matrix generated in Stage 1.

Generally, for an arbitrary scattering process described by the scattering matrix $[S]$, the measured scattering matrices at the two antenna positions (see Fig. 11) are given by the following congruent transformations:

$$[S_1] = [P_{21}][S][P_{21}]^T \quad \text{and} \quad [S_2] = [P_{22}][S][P_{22}]^T. \quad (35)$$

Equation (35) can be rewritten in terms of the 4-D scattering vectors as

$$\underline{k}_1 = [P_{41}]\underline{k} \quad \text{and} \quad \underline{k}_2 = [P_{42}]\underline{k} \quad (36)$$

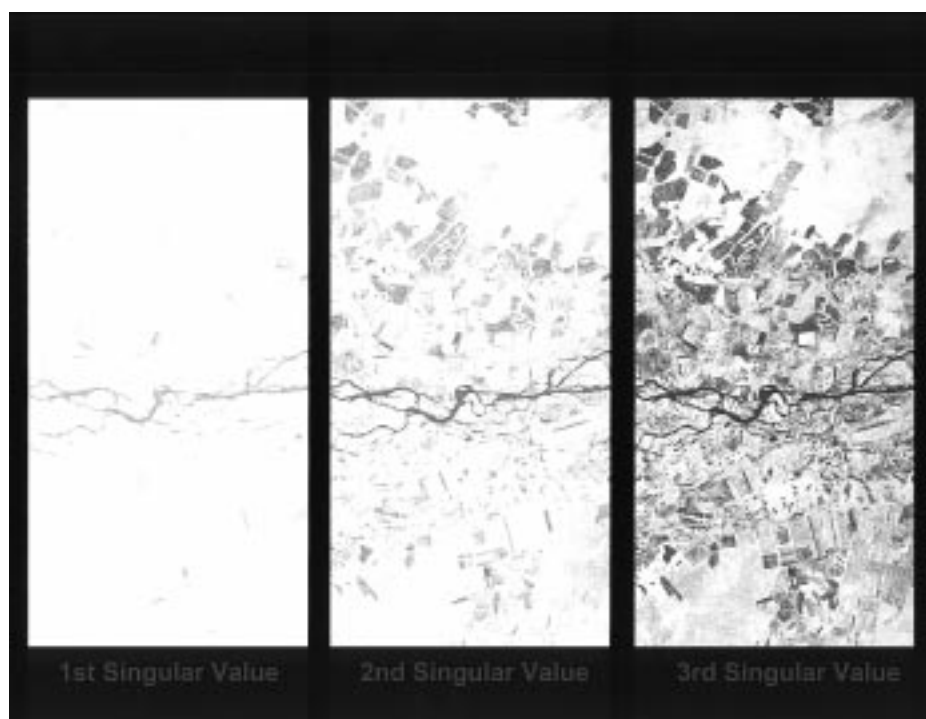
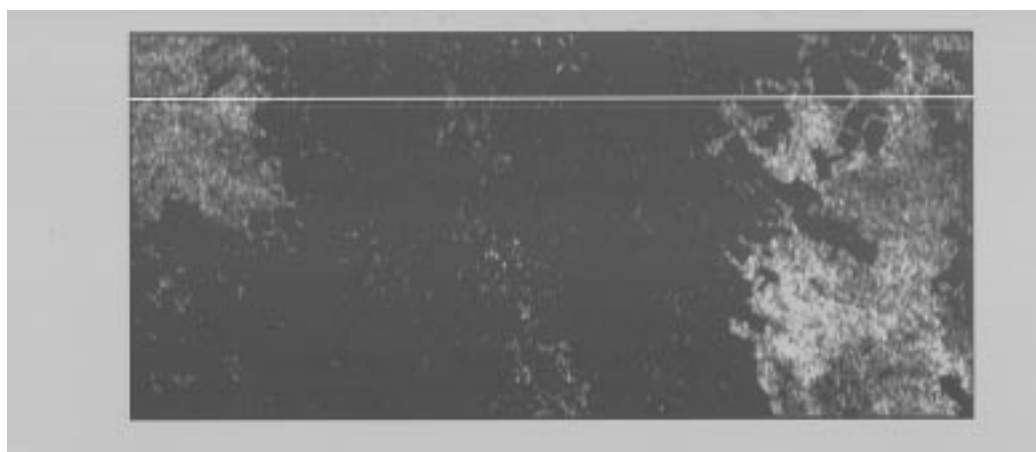
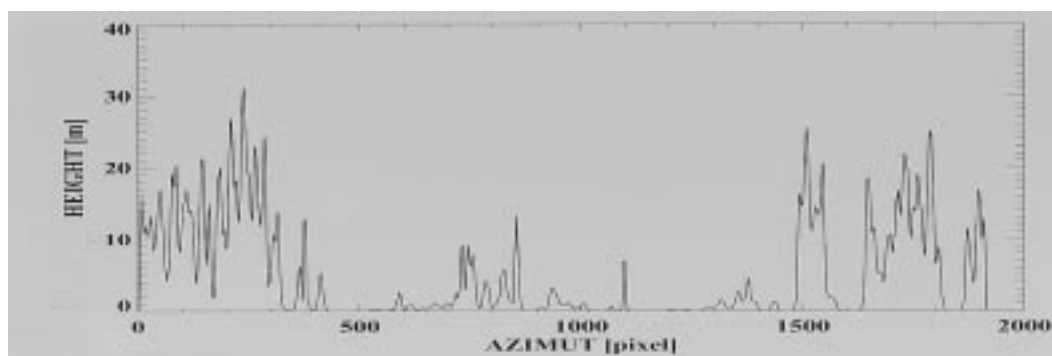


Fig. 7. Coherence maps of interferograms generated by using the optimum scattering mechanisms related to the first (left), second (middle), and third singular value (right).



(a)



(b)

Fig. 8. Phase difference between the effective phase scattering centers of the forested areas. (a) Phase image of the whole area and (b) rescaled height profile corresponding to the marked azimuth line.



Fig. 9. Three-dimensional representation of the height difference between effective phase scattering centers of the forested areas.

where $[P_{4i}]$ are 4×4 complex matrices describing anisotropic propagation effects on the scattering vectors [36]. Applying (36) for the scatterer configuration of the model, as shown in Fig. 10(a), we obtain the following formal expressions for the elements of the matrix $[T_8]$:

$$[T_8] = \begin{bmatrix} [T_{11}] & [\Omega_{12}] \\ [\Omega_{12}]^{*T} & [T_{22}] \end{bmatrix} = \left\langle \begin{bmatrix} \underline{k}_1 \\ \underline{k}_2 \end{bmatrix} \begin{bmatrix} \underline{k}_1^{*T} & \underline{k}_2^{*T} \end{bmatrix} \right\rangle \quad (37)$$

where

$$\begin{aligned} \underline{k}_1 &= [P_{41}(\underline{r})]\underline{k}_T + \int_V [P_{41}(\underline{r})]\underline{k}(\underline{r}) d\underline{r} \\ \underline{k}_2 &= [P_{42}(\underline{r})]\underline{k}_T + \int_V [P_{42}(\underline{r})]\underline{k}(\underline{r}) d\underline{r}. \end{aligned} \quad (38)$$

Using the simplest scalar approximation for propagation through the canopy [36], $[P_4]$ reduces to a complex scalar times the identity matrix. In this case, we can simplify (38) and obtain the following form for the 3-D complex vectors \underline{k}_1 and \underline{k}_2 :

$$\begin{aligned} \underline{k}_1 &= \exp(2\underline{\kappa}r_{T1})\underline{k}_T + \int_V \exp(2\underline{\kappa}r_1)\underline{k}(\underline{r}_1) d\underline{r}_1 \\ \underline{k}_2 &= \exp(2\underline{\kappa}r_{T2})\underline{k}_T + \int_V \exp(2\underline{\kappa}r_2)\underline{k}(\underline{r}_2) d\underline{r}_2. \end{aligned} \quad (39)$$

Using this simplified form, we can now use (37) to evaluate the reduced matrix $[T_6]$. Note that \underline{k} in (39) is the complex wavenumber for propagation, representing both attenuation and phase shifts in the medium.

There remain two key issues to be resolved before we can evaluate $[T_6]$: 1) the first is purely geometrical and involves

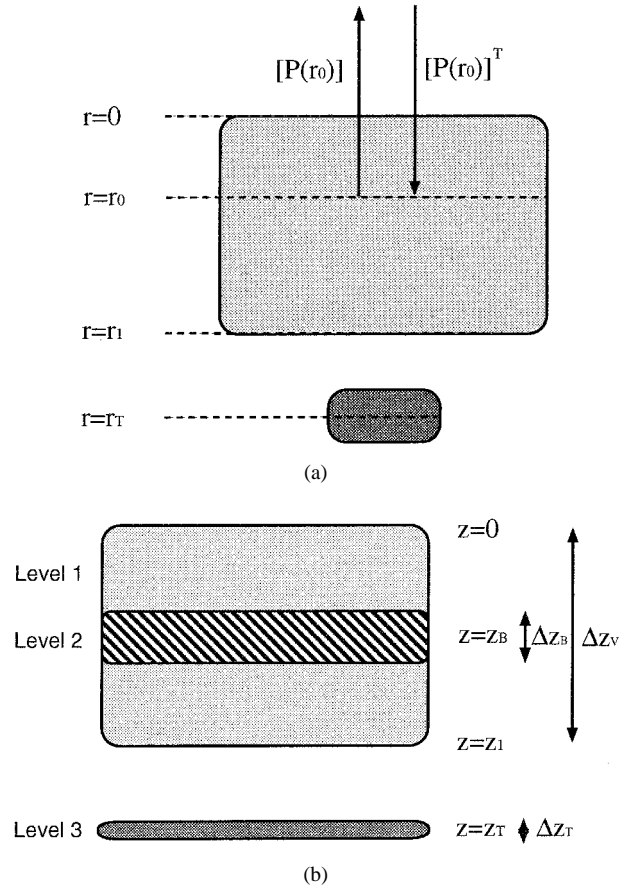


Fig. 10. (a) Schematic representation of the simplified scattering model and (b) three-level configuration of the forest scattering model.

calculation of an effective propagation constant based on the range difference $\Delta r = r_2 - r_1$ and its relation to the surface coordinates shown in Fig. 11 and 2) the second involves evaluation of the statistical polarimetric averaging implicit in the $\langle \dots \rangle$ brackets in (37). In the following, we deal with these two issues separately.

A. Effective Propagation Constant

The first problem is to relate the change in range throughout the scattering volume to the baseline radar coordinates and a reference surface coordinate system. Fig. 11 shows the geometry, in which (m, n) are the radar range and cross-range coordinates and (z, y) is the surface reference system. B_n is the normal component of the baseline, and the angle θ is the mean angle of incidence onto the surface.

When we use (39) to evaluate $[T_6]$, the conventional coherency matrices $[T_{11}]$ and $[T_{22}]$ are not sensitive to the imaginary part of the propagation constant $\text{Im}\{\kappa\}$ but only to the real part $\text{Re}\{\kappa\}$, which causes attenuation of the wave as it propagates. On the other hand, the off-diagonal matrix $[\Omega_{12}]$ involves complex scalars of the form $\exp(-i \text{Im}\{\kappa\} \Delta r)$. It is just such terms that we wish to exploit since they give rise to sensitivity to small height changes in the scatterer position.

Assuming $R \gg B_n$, we can employ a small angle approximation $\delta\theta \approx \sin \delta\theta = B_n/R$ and the complex phase term

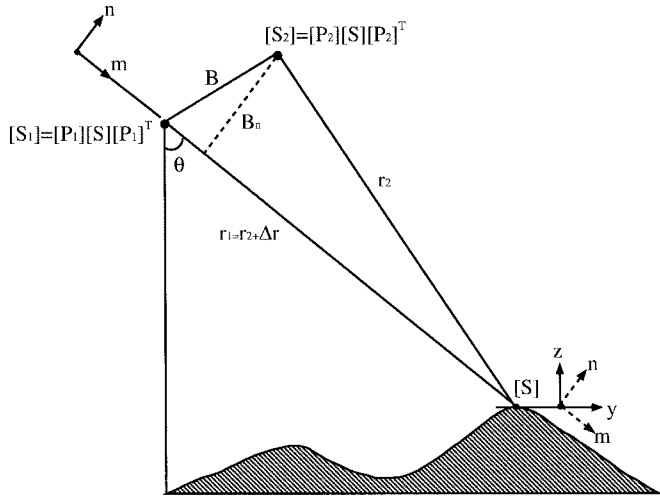


Fig. 11. Interferometric geometry with baseline (m, n) and surface (y, z) coordinate systems.

has the simplified form

$$\exp\left(\frac{4\pi\delta\theta}{\lambda}m\right) \approx \exp\left(\frac{4\pi B_n}{\lambda R}m\right). \quad (40)$$

Note that for simplicity we are ignoring noise and temporal decorrelation effects and considering only the effects of baseline decorrelation. Noise will have no polarimetric structure and so remains unchanged in its analysis from scalar theories. Temporal decorrelation is an important effect in repeat-pass interferometry that we will consider in a separate paper.

Now transforming to the surface reference coordinates we can express (40) in the modified form $\exp(-i\phi(y, z))$, where

$$\phi(y, z) = y\left(\frac{2\text{Im}\{\kappa\}B_n \cos \theta}{R} - 2\Delta\kappa \sin \theta\right) + z\left(\frac{2\text{Im}\{\kappa\}B_n \cos \theta}{R} + 2\Delta\kappa \sin \theta\right) \quad (41)$$

and we have also included the possibility of making a wavenumber shift $\Delta\kappa$ between the two images. As is apparent from (41), we can always remove the y -dependence of the phase ϕ by choosing $\Delta\kappa$ based on the geometry of the system so that

$$\Delta\kappa = \frac{\text{Im}\{\kappa\}B_n}{R \tan \theta}. \quad (42)$$

In this case, the interferometric coherence depends only on the height distribution above the reference plane. To study decorrelation in the z -direction only, we define an effective propagation constant using (41) and (42) so that

$$\kappa_z = \frac{2\text{Im}\{\kappa\}B_n}{R \sin \theta}. \quad (43)$$

In this way, the model can be reduced to a 1-D model for wave propagation through a canopy. By employing a change of wavenumber between \underline{k}_1 and \underline{k}_2 , according to (42), we can then study the polarimetric coherence properties of such a medium.

B. Polarimetric Volume Statistics

In the analysis above, we showed that under a scalar approximation, propagation effects may be reduced through suitable signal processing to a simple scalar shift in wavenumber. This is already well analyzed in the literature [19], [20]. However, the polarimetric behavior of the canopy depends on the statistics of the scattering vector \underline{k} , as a function of height z . This behavior governs the polarization dependence of coherence and so is of prime concern to us. In this section, we outline a model for such behavior.

The model is a three-layer configuration, as shown in Fig. 10(b), and comprises the following elements.

- **Level 1:** The canopy is modeled as a cloud of electrically small anisotropic particles with random orientation distribution. The particle shape may be varied from prolate (needles and twigs) through spherical to oblate (leaves). The position of these particles is assumed to be uniformly distributed in the range from $z = 0$ to $z = z_1$. This model gives rise to a random vector \underline{k}_V defined as

$$\underline{k}_V = [U(\vartheta)]\underline{k}_P = a_P \begin{bmatrix} 1 & 0 & 0 \\ 0 & \cos \vartheta & \sin \vartheta \\ 0 & -\sin \vartheta & \cos \vartheta \end{bmatrix} \begin{bmatrix} \cos \alpha_P \\ \sin \alpha_P \\ 0 \end{bmatrix} \quad (44)$$

where ϑ is a random variable (orientation of the particles) and α_P is a deterministic parameter governing the shape. The simplest approximation for ϑ is to be uniformly distributed in the range zero to π , but alignment of particles can also be accommodated by the model.

- **Level 2:** Within the canopy, we assume there is a spatially localized scatterer representing the fixed branch/trunk structure. This scatterer is modeled by a deterministic scattering mechanism \underline{k}_B

$$\underline{k}_B = a_B \begin{bmatrix} \cos \alpha_B \\ \sin \alpha_B \cos \beta_B \\ \sin \alpha_B \sin \beta_B \end{bmatrix} \quad (45)$$

where again α_B determines the type of scattering mechanism and β_B determines the fixed orientation of the scatterer. The scatterer position is assumed to be at $z = z_1/2$ with a uniform variation $\Delta z \ll 1$.

- **Level 3:** Beneath the canopy, we model the effects of the ground or ground-trunk interaction by locating another scattering mechanism \underline{k}_T

$$\underline{k}_T = a_T \begin{bmatrix} \cos \alpha_T \\ \sin \alpha_T \cos \beta_T \\ \sin \alpha_T \sin \beta_T \end{bmatrix}. \quad (46)$$

This can be any scattering mechanism, ranging from a Bragg surface model to a dielectric dihedral mechanism corresponding to ground-trunk multiple scattering effects. Also assumed here is that this scatterer is located at $z = z_T + \Delta z_T$, where $\Delta z_T \ll z_T$.

Note that propagation attenuation effects are simply modeled at this stage by varying the relative amplitudes a_P , a_B , and a_T .

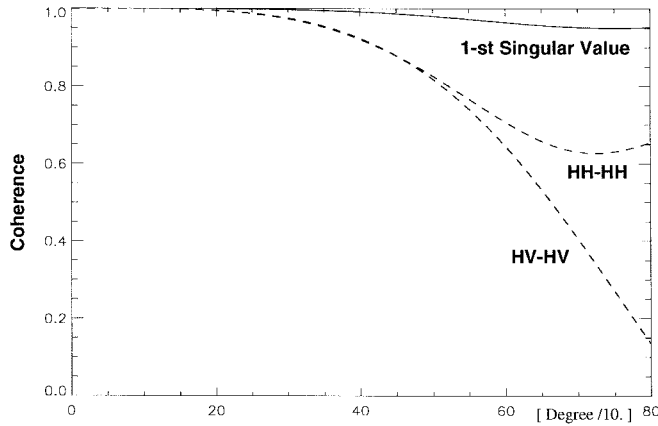


Fig. 12. Coherence as a function of the antenna look-angle difference $\Delta\theta$ for different interferograms.

This 1-D random model may be used in various forms for numerical Monte Carlo simulation of polarimetric interferometry data. We will use it here to give two examples related to the two main new ideas proposed in this paper: coherence optimization and the coherent scattering decomposition. To demonstrate why polarization can make such a significant difference to the interferometric coherence, we simulate a volume plus point-scatterer scenario by using a simplified configuration of the model [see Fig. 10(a)] and apply the optimization algorithm to this configuration. We simulate the volume as a cloud of dipoles ($\alpha_P = 45^\circ$) with equally distributed orientation about the radar line of sight between zero and π and the hidden scatterer as a dihedral anisotropic scattering mechanism ($\alpha_T = 75^\circ$). The coherence as a function of the antenna look-angle difference $\Delta\theta$, which is directly proportional to the normal component of the baseline for a given range, is shown in Fig. 12. The interferometric coherence between the conventional polarizations in the (H, V)-basis decreases with increasing $\Delta\theta$ as a consequence of the increasing contribution of volume decorrelation. On the other hand, the optimized coherence shows a $\Delta\theta$ independent behavior with a value close to one, as expected for a deterministic point scatterer. The corresponding optimum scattering mechanism $\underline{w}_{\text{opt}}$ can be further directly identified as an anisotropic dihedral scattering process: $\alpha \approx 75^\circ$. This indicates that the optimization algorithm has successfully separated the backscattering contribution of the deterministic point scatterer from the volume-scattering contribution that introduces the phase-noise.

In a second example, we illustrate how the decomposition into a set of coherent scattering mechanisms can be used to determine the height difference between their effective scattering phase centers. To do this, we use the model in its three-level configuration and set the branch scattering mechanism \underline{k}_B to be orthogonal to those of the ground \underline{k}_T (i.e., $\underline{k}_B^{*T} \underline{k}_T = 0$). Using a fixed baseline $\Delta\theta = 2.5^\circ$, we vary continuously the distance between the branch and the ground layer. The height difference evaluated from the phase difference between the interferograms formed by using the scattering mechanisms extracted with the decomposition analysis of (32) is shown in Fig. 13. The evaluation of the

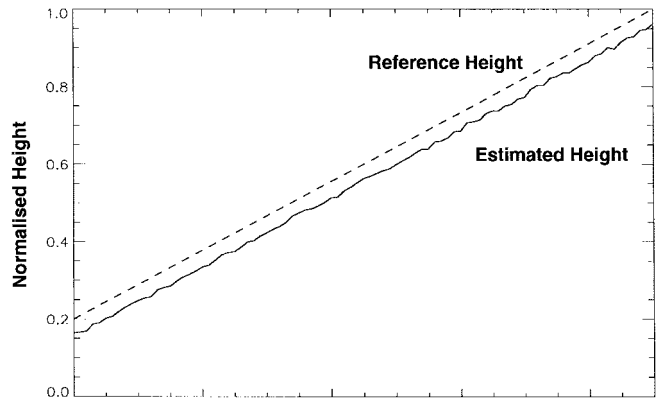


Fig. 13. Height difference between scattering mechanisms extracted using the interferometric decomposition compared with the "true" height difference.

height difference arises from the orthogonality of the scattering mechanisms in the branch and ground layers. The fact that for real forest the effective scattering mechanisms are orthogonal and located at different heights (ground—branches—canopy top) enables us, using the proposed decomposition, to estimate their height difference. It is just such an effect that we propose for the interpretation of Fig. 8.

VIII. CONCLUSIONS

In this paper, we have derived a general formulation for coherent interferometry using polarized waves. Based on this formulation, we have solved the coherence optimization problem to obtain the optimum scattering mechanisms that lead to the best phase estimates. Comparison with conventional single-polarization estimates illustrates the significant processing gains that are possible if we have access to full polarimetric interferometric data.

We have introduced a new coherent decomposition theorem for interferometric applications based on the singular value spectrum of a 3×3 complex matrix that allows us to decompose polarimetric interferometric problems into a set of coherent scattering mechanisms. As a consequence, we are able to generate interferograms related to certain independent scattering mechanisms and extract the height differences between them. The limitation of this technique is the existence of independent scattering mechanisms located at different height positions.

To explain the physical origin of these mechanisms, we have further developed a coherent electromagnetic scattering model. In addition, the model can be used to establish the suitability of the decomposition algorithm for solving the problem of estimating the location of the effective scattering center, which is a critical point in the physical interpretation of interferograms.

The perceptions gained from the model, combined with the results of the application of the decomposition algorithm to SIR-C data, allow us to propose that polarimetric interferometry using single-frequency scattering matrix interferometric data is a very promising technique for the extraction of important forest and other volume-scattering parameters. The fact that forest backscattering consists of different scattering

processes at different heights makes this possible. The main requirement is to obtain canopy penetration, and so use of full polarimetric sensors operating at a lower frequencies, such as L-band, is preferred. The extension of polarimetric interferometry to wideband systems is a challenge, especially for applications related to ground-penetration imaging.

The price to be paid for the improvements that arise from the introduction of polarimetry in interferometric processing is that fully coherent polarimetric data must be collected; only then can scattering mechanisms be separated.

APPENDIX A

INTERPRETATION OF POLARIMETRIC SCATTERING MECHANISMS

We will show here how complex normalized vectors may be used to represent an arbitrary polarimetric scattering mechanism. We can then generate the projection or coherent decomposition of a scattering matrix into a set of general canonical mechanisms. For a given symmetric scattering matrix $[S]$

$$[S] = \begin{bmatrix} a & b \\ b & c \end{bmatrix} \quad (47)$$

the corresponding reduced scattering vector \underline{k} in the Pauli matrix basis [13] can be written as

$$\underline{k} = \frac{1}{\sqrt{2}} [a + c, a - c, 2b]^T = |\underline{k}\rangle \underline{w} \quad (48)$$

where \underline{w} is a unitary complex vector. The general form of \underline{w} is given by [22]

$$\underline{w} = \begin{bmatrix} \cos \alpha \exp i\phi \\ \sin \alpha \cos \beta \exp i\delta \\ \sin \alpha \sin \beta \exp i\gamma \end{bmatrix}. \quad (49)$$

This leads to the following important *Scattering Vector Reduction Theorem*: it is always possible to reduce an arbitrary scattering mechanism, represented by a complex unitary vector \underline{w} to the identity $[1, 0, 0]^T$ by the following set of ordered matrix transformations:

$$\begin{bmatrix} 1 \\ 0 \\ 0 \end{bmatrix} = \begin{bmatrix} \cos \alpha & \sin \alpha & 0 \\ -\sin \alpha & \cos \alpha & 0 \\ 0 & 0 & 1 \end{bmatrix} \begin{bmatrix} 1 & 0 & 0 \\ 0 & \cos \beta & \sin \beta \\ 0 & -\sin \beta & \cos \beta \end{bmatrix} \cdot \begin{bmatrix} \exp(-i\phi) & 0 & 0 \\ 0 & \exp(-i\delta) & 0 \\ 0 & 0 & \exp(-i\gamma) \end{bmatrix} \underline{w}. \quad (50)$$

The third matrix represents a set of scattering phase angles, while the first and second are mathematically canonical forms of plane rotations. Physically, only one of them β corresponds to a physical rotation of the sensor coordinates. An important point to note is that, as long as we use the Pauli basis for the vectorization of the scattering matrix, β represents physically the orientation of the scatterer about the radar line of sight. This correspondence follows directly from the nature of the Pauli matrices, which relate rotations to matrix transformations, as first shown in [13].

The second parameter α is not associated with a physical rotation but represents an internal degree of freedom of the scatterer. It is continuous with a useful range of $0^\circ \leq \alpha \leq 90^\circ$

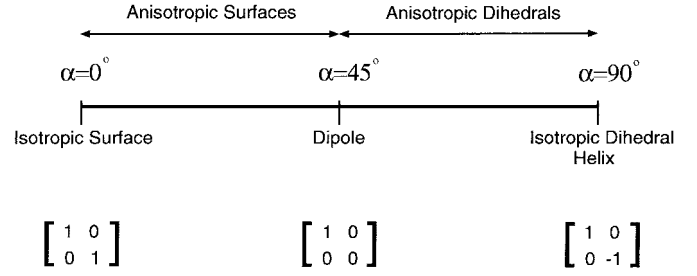


Fig. 14. Schematic representation of the α -angle interpretation.

and associated with the “type” of scattering mechanism. When $\alpha = 0^\circ$ we have an isotropic surface and $\alpha = 90^\circ$, we have an isotropic dihedral or a helix. For intermediate values of α , we can represent anisotropic scattering mechanisms in which $|HH|$ and $|VV|$ are no longer equal (as they are for $\alpha = 0^\circ$ and $\alpha = 90^\circ$). In the limit of $\alpha = 45^\circ$, we have a dipole scatterer in which one of the copolarized scattering coefficients goes to zero. The range of possible variations in scattering mechanism can be represented by the variation of α along the real line, as shown in Fig. 14 [23].

It is important to note that the scatterer is identified independently of its orientation β , so it does not matter if there is a misalignment between radar and scatterer coordinates.

APPENDIX B

SINGULAR VALUE INTERPRETATION OF THE OPTIMIZATION ALGORITHM

If we write the two Hermitian positive, semidefinite matrices $[T_{11}]$ and $[T_{22}]$ in terms of their eigenvalue decompositions [15], they and their inverses can be expressed in terms of square root matrices

$$\begin{aligned} [T_{jj}] &= [U_j]^* [T_{jj}] [U_j] \\ &= [U_j]^* \sqrt{[\Sigma_j]} \sqrt{[\Sigma_j]} \\ [U_j] &= \sqrt{[T_{jj}]}^* \sqrt{[T_{jj}]} \\ [T_{jj}]^{-1} &= [U_j]^* [T_{jj}]^{-1} [U_j] \\ &= [U_j]^* \sqrt{[\Sigma_j]^{-1}} \sqrt{[\Sigma_j]^{-1}} \\ [U_j] &= \sqrt{[T_{jj}]^{-1}}^* \sqrt{[T_{jj}]^{-1}} \end{aligned} \quad (51)$$

where $j = 1$ or 2 , $[U_j]$ are the matrices of eigenvectors, and $[\Sigma_j]$ are diagonal matrices with the real nonnegative eigenvalues along the diagonal. The significance of this result lies in the fact that we can transform the complex vector \underline{k} to a new basis defined by

$$\underline{k}'_j = \sqrt{[\Sigma_j]} [U_j] \underline{k}_j = \sqrt{[T_{jj}]} \underline{k}_j. \quad (52)$$

This represents a shift into the orthogonal scattering mechanisms represented by the eigenvector matrix $[U_j]$, amplitude-weighted by the reciprocal of their respective eigenvalues. Physically, this represents a whitening process for the vector \underline{k} .

We now apply the same transformation to (28) to obtain for the optimum weight vector \underline{w}_2 the modified equation with

$$\begin{aligned}
\mathbf{w}'_2 &= \sqrt{[T_{22}]} \mathbf{w}_2 \\
[T_{22}]^{-1} [\Omega_{12}]^* \sqrt{[T_{11}]^{-1}}^* \sqrt{[T_{11}]^{-1}} [\Omega_{12}] \sqrt{[T_{22}]^{-1}} \mathbf{w}'_2 \\
&= \nu \sqrt{[T_{22}]^{-1}} \mathbf{w}'_2 \Rightarrow \\
\sqrt{[T_{22}]} [T_{22}]^{-1} [\Omega_{12}]^* \sqrt{[T_{11}]^{-1}}^* \sqrt{[T_{11}]^{-1}} [\Omega_{12}] \sqrt{[T_{22}]^{-1}} \mathbf{w}'_2 \\
&= \nu \mathbf{w}'_2 \Rightarrow \\
\left(\sqrt{[T_{22}]^{-1}} [\Omega_{12}]^* \sqrt{[T_{11}]^{-1}}^* \right) \\
\cdot \left(\sqrt{[T_{11}]^{-1}} [\Omega_{12}] \sqrt{[T_{22}]^{-1}} \right) \mathbf{w}'_2 \\
&= \nu \mathbf{w}'_2. \tag{53}
\end{aligned}$$

Defining the 3×3 complex matrix $[\Pi] := \sqrt{[T_{11}]^{-1}} [\Omega_{12}] \sqrt{[T_{22}]^{-1}}$, we obtain from (53)

$$[\Pi]^* [\Pi] \mathbf{w}'_2 = \nu \mathbf{w}'_2. \tag{54}$$

Equation (54) is a classical Hermitian eigenvalue problem for the eigenvectors \mathbf{w}'_2 . The eigenvalues ν_i of the Hermitian positive, semidefinite matrix $[\Pi]^* [\Pi]$ are real and nonnegative, and the eigenvectors \mathbf{w}'_2 are orthonormal. The relation between $[\Pi]^* [\Pi]$ and $[T_{11}]^{-1} [\Omega_{12}] [T_{22}]^{-1} [\Omega_{12}]^*$ is given by following similarity transformation:

$$\begin{aligned}
[T_{11}]^{-1} [\Omega_{12}] [T_{22}]^{-1} [\Omega_{12}]^* \\
= \sqrt{[T_{22}]^{-1}} [\Pi]^* [\Pi] \sqrt{[T_{22}]} \tag{55}
\end{aligned}$$

and therefore $[T_{11}]^{-1} [\Omega_{12}] [T_{22}]^{-1} [\Omega_{12}]^*$ must have the same eigenvalues ν_i as the complex matrix $[\Pi]^* [\Pi]$.

Hence, we have shown that the eigenvalues in (28) are real and that the optimum value of the Lagrangian function L therefore corresponds to the maximum eigenvalue ν . Note that in (54) we are essentially solving the optimization problem in a basis in which $[T_6]$ has the special form

$$[\tilde{T}_6] = \begin{bmatrix} [I_3] & [\Pi] \\ [\Pi]^* & [I_3] \end{bmatrix} \tag{56}$$

where $[I_3]$ is a 3×3 identity matrix and $[\Pi]$ is defined in (53). In this case, the modified Lagrangian function is

$$L = \mathbf{w}_1^* [\Pi] \mathbf{w}_2 + \lambda_1 (\mathbf{w}_1^* \mathbf{w}_1 - C_1) + \lambda_2 (\mathbf{w}_2^* \mathbf{w}_2 - C_2). \tag{57}$$

The optimum values of interferometric coherence are then given by the singular values of the matrix $[\Pi]$.

Physically, the above transformations correspond to the following operations on the complex scattering vectors in both images.

- 1) Formation of the coherency matrix $[T_{11}]$ ($[T_{22}]$) by forming the average Hermitian positive, semidefinite outer product of the scattering vector \mathbf{k}_1 (\mathbf{k}_2) from Image 1 (2) and transforming it into its characteristic scattering mechanisms (eigenvector target decomposition), weighting the amplitudes of these scattering mechanisms by the reciprocal of their corresponding eigenvalue.
- 2) Generation of the matrix $[\Pi]$ as the complex cross correlation between the weighted scattering mechanisms in Images 1 and 2. This 3×3 complex matrix will generally be of full rank and non-Hermitian.

- 3) Application of an SVD decomposition to the matrix $[\Pi]$. This corresponds to finding two scattering mechanisms, one in Image 1 (right singular vector) and a different one in Image 2 (left singular vector), which are formed as a linear combination of the dominant target scattering mechanisms in each image.
- 4) Projection of the scattering matrix data from Image 1 (2) onto the optimum scattering mechanism for Image 1 (2) derived in the last step and formation of an interferogram between these two complex scalar images. This interferogram will then have the highest possible coherence.

ACKNOWLEDGMENT

The authors would like to thank W. Keydel, E. Lüneburg, and W.-M. Boerner for their helpful discussions and support and A. Moreira, A. Reigber, and D. Eagles for reading the manuscript and for their many constructive comments.

REFERENCES

- [1] L. C. Graham, "Synthetic interferometric radar for topographic mapping," *Proc. IEEE*, vol. 62, pp. 763–768, June 1974.
- [2] H. A. Zebker and R. M. Goldstein, "Topographic mapping from interferometric synthetic aperture radar observations," *J. Geophys. Res.*, vol. 91, pp. 4993–4999, Apr. 1986.
- [3] H. A. Zebker and J. Villasenor, "Decorrelation in interferometric radar echos," *IEEE Trans. Geosci. Remote Sensing*, vol. 30, pp. 950–959, July 1992.
- [4] A. Reigber, "Multitemporale Analyse der Kohärenz von SAR Daten," Diploma thesis, Univ. Constance, Germany, 1997.
- [5] K. P. Papathanassiou and A. Reigber, "On the interferometric coherence: A multifrequency and multitemporal analysis," in *Proc. FRINGE'96 Workshop*, ESA, Zurich, Switzerland, pp. 319–330.
- [6] R. N. Treuhart, S. N. Madsen, M. Moghaddam, and J. J. van Zyl, "Vegetation characteristics and underlying topography from interferometric data," *Radio Sci.*, vol. 31, pp. 1449–1495, Nov./Dec. 1996.
- [7] J. O. Hagberg, L. M. Ulander, and J. Askne, "Repeat-pass interferometry over forested terrain," *IEEE Trans. Geosci. Remote Sensing*, vol. 33, pp. 331–340, Mar. 1995.
- [8] J. Askne, P. B. Dammert, L. M. Ulander, and G. Smith, "C-band repeat-pass interferometric SAR observations of the forest," *IEEE Trans. Geosci. Remote Sensing*, vol. 35, pp. 25–35, Jan. 1997.
- [9] R. Lanari, G. Fornaro, D. Riccio, M. Migliaccio, K. P. Papathanassiou, J. R. Moreira, M. Schwabisch, L. Dutra, G. Puglisi, G. Franceschetti, and M. Coltelli, "Generation of digital elevation models by using SIR-C/X-SAR multifrequency two-pass interferometry: The Etna case study," *IEEE Trans. Geosci. Remote Sensing*, vol. 34, pp. 1097–1114, Sept. 1996.
- [10] J. S. Lee, M. R. Grunes, and R. Kwok, "Intensity and phase statistics of multilook polarimetric and interferometric SAR imagery," *IEEE Trans. Geosci. Remote Sensing*, vol. 32, pp. 68–78, Jan. 1994.
- [11] J. J. van Zyl and C. F. Brumette, "Bayesian classification of polarimetric SAR images using adaptive *a priori* probabilities," *Int. J. Remote Sensing*, vol. 13, pp. 835–840, 1992.
- [12] E. Rignot and R. Chellappa, "Segmentation of polarimetric synthetic aperture radar data," *IEEE Trans. Image Processing*, vol. 1, pp. 281–300, 1992.
- [13] R. J. Huynen, "Phenomenological theory of radar targets," Ph.D. dissertation, Tech. Univ. Delft, The Netherlands, 1970.
- [14] J. J. van Zyl, "Unsupervised classification of scattering behavior using radar polarimetry data," *IEEE Trans. Geosci. Remote Sensing*, vol. 27, pp. 36–45, Jan. 1990.
- [15] S. R. Cloude and E. Pottier, "A review of target decomposition theorems in radar polarimetry," *IEEE Trans. Geosci. Remote Sensing*, vol. 34, pp. 498–518, Mar. 1996.
- [16] D. L. Schuler, J. S. Lee, and G. De Grandi, "Measurement of topography using polarimetric SAR images," *IEEE Trans. Geosci. Remote Sensing*, vol. 34, pp. 1266–1277, Sept. 1996.

- [17] D. Just and R. Bamler, "Phase statistics of interferograms with applications to synthetic aperture radar," *Appl. Opt.*, vol. 33, pp. 4361–4368, July 1994.
- [18] C. Prati and F. Rocca, "Improving slant-range resolution with multiple SAR surveys," *IEEE Trans. Aerosp. Electron. Syst.*, vol. 29, pp. 135–143, Jan. 1993.
- [19] F. Gatelli, A. Monti-Guarnieri, F. Parizzi, P. Pasquali, C. Prati, and F. Rocca, "The wavenumber shift in SAR interferometry," *IEEE Trans. Geosci. Remote Sensing*, vol. 32, pp. 855–865, July 1994.
- [20] C. Prati, F. Rocca, A. Monti-Guarnieri, and P. Pasquali, "Measuring volumetric scattering effects with SAR interferometry," in *Proc. PIERS'94*, ESA, Noordwijk, The Netherlands, 1994 (only available on CD ROM).
- [21] J. J. van Zyl, H. A. Zebker, and C. Elachi, "Imaging radar polarization signatures: Theory and observation," *Radio Sci.*, vol. 22, pp. 529–543, 1987.
- [22] S. R. Cloude and E. Pottier, "Concept of polarization entropy in optical scattering," *Opt. Eng.*, vol. 34, no. 6, pp. 1599–1610, 1995.
- [23] ———, "An entropy based classification scheme for land applications of polarimetric SAR," *IEEE Trans. Geosci. Remote Sensing*, vol. 35, pp. 68–78, Jan. 1997.
- [24] E. Lüneburg, "Principles in radar polarimetry: The consimilarity transformation of radar polarimetry versus the similarity transformations in optical polarimetry," *IEICE Trans. Electron.*, Special Issue on Electromagnetic Theory, vol. E-78C, no. 10, pp. 1339–1345, 1995.
- [25] W.-M. Boerner, "Polarimetry in remote sensing and imaging of terrestrial and planetary environments," in *Proc. 3rd Int. Workshop Radar Polarimetry (JIPR'95)*, IRESTE, University of Nantes, France, vol. 1, pp. 1–38.
- [26] ———, "Polarization dependence in electromagnetic inverse problems," *IEEE Trans. Antennas Propagat.*, vol. AP-29, pp. 262–274, Feb. 1981.
- [27] K. P. Papathanassiou and J. R. Moreira, "Interferometric analysis of multifrequency and multipolarization SAR data," in *Proc. IEEE IGARSS'96*, Lincoln, NE, vol. III, pp. 1227–1229.
- [28] J. J. van Zyl, "Calibration of polarimetric radar images using only image parameters and trihedral corner reflector responses," *IEEE Trans. Geosci. Remote Sensing*, vol. 28, pp. 337–348, May 1990.
- [29] D. J. Klein and A. Freeman, "Quadpolarization SAR calibration using target reciprocity," *J. Electromagn. Waves Applicat.*, vol. 5, no. 7, pp. 735–751, 1991.
- [30] S. Quegan, "A unified algorithm for phase and cross-talk calibration of polarimetric data—Theory and observations," *IEEE Trans. Geosci. Remote Sensing*, vol. 32, pp. 89–99, Jan. 1994.
- [31] W.-M. Boerner, C. L. Liu, and X. Zhang, "Comparison of optimization procedures for 2×2 sinclair, 2×2 graves, 3×3 covariance, and 4×4 Mueller (symmetric) matrices in coherent radar polarimetry and its application to target versus background discrimination in microwave remote sensing," *EARSeL Adv. Remote Sensing*, vol. 2, pp. 55–82, 1991.
- [32] I. Novak, M. C. Burl, and W. W. Irving, "Optimal polarimetric processing for enhanced target detection," *IEEE Trans. Aerosp. Electron. Syst.*, vol. 29, pp. 234–244, Jan. 1993.
- [33] E. Krogager, "A new decomposition of the radar target scattering matrix," *Electron. Lett.*, vol. 26, no. 18, pp. 1525–1526, 1990.
- [34] K. Sarabandi and Y. C. Lin, "Simulations of interferometric SAR response for characterizing the scattering phase center statistics of forest canopies," submitted for publication.
- [35] ———, "Simulations of interferometric SAR response to deciduous and coniferous forest stands," in *Proc. IEEE IGARSS'97*, Singapore, vol. IV, pp. 1887–1889.
- [36] S. R. Cloude and K. P. Papathanassiou, "Polarimetric radar interferometry," in *Proc. SPIE'97, SPIE's 42nd Annu. Mtg.*, vol. 3120, in *Wideband Interferometric Sensing and Imaging Polarimetry*, San Diego, CA, July 1997.
- [37] W.-M. Boerner *et al.*, "Polarimetry in radar remote sensing: Basic and applied concept," in *Manual of Remote Sensing: Principles and Applications of Imaging Radar*, vol. 8, 3rd ed, F. M. Henderson and A. J. Lewis, Eds. New York, Wiley, 1998, ch. 5.

Shane Robert Cloude (M'88) received the B.Sc. degree from the University of Dundee, U.K., in 1981 and the Ph.D. degree from the University of Birmingham, U.K., in 1987.

He held teaching and research posts at the University of Dundee and the University of York, U.K. He was an Associate Professor at IRESTE, which is an engineering school of the University of Nantes, France. He is currently with Applied Electromagnetics, St. Andrews Fife, U.K. He has published more than 50 research papers, mainly on the subject of electromagnetic scattering and polarimetry. His main current research interests are in active remote sensing, radar imaging techniques, and time-domain methods for computational electromagnetics.

Dr. Cloude is a Chartered Engineer and a member of the Electromagnetic Academy, Optical Society of America (OSA), and the Institute of Electrical Engineers.

Konstantinos P. Papathanassiou, for a photograph and biography, see this issue, p. 1465.